Journal of Materials Chemistry A

ROYAL SOCIETY OF CHEMISTRY

PAPER

View Article Online
View Journal | View Issue

Cite this: J. Mater. Chem. A, 2024, 12, 4086

Electrochemical surface reconstruction of nickel cobalt pyrophosphate to Ni/Co-hydroxide-(oxy) hydroxide: an efficient and highly durable battery-type supercapacitor electrode material†

Avishek Roy,[a] Harish Reddy Inta,[ab] Sourav Ghosh,[a] Heramba V. S. R. M. Koppisetti,[a] Ayan Mondal,[a] Bhagwat Ram Verma,[a] Saikat Bag[a] and Venkataramanan Mahalingam *[a]

Developing transition metal-based electrode materials with high charge storage ability and excellent cycle life is a substantial challenge for supercapacitor applications. This report demonstrates an improved specific capacitance and excellent cycling stability for a Ni/Co-hydroxide-(oxy)hydroxide electrode material obtained from the electrochemical reconstruction of a Ni/Co-pyrophosphate precursor. Herein, we have prepared a series of nickel/cobalt pyrophosphate (Ni_xCo_{100-x} 600) (x = 90, 80, 70, 60, 50, 0) materials through a simple co-precipitation method followed by thermal annealing. Upon electrochemical treatment, the developed nickel/cobalt pyrophosphate materials were transformed into porous Ni/Co-hydroxide-(oxy)hydroxides. This is due to the etching of pyrophosphate anions with electrochemical cycling, confirmed by rigorous physical characterization. Among them, Ni-rich electrodes showed higher specific capacitance values due to the dominant intercalation redox behavior (battery-type storage), yet they suffer from poor cycle stability. In contrast, Co-rich electrodes display low specific capacitance and excellent capacitance retention as the charge storage mainly occurs through surface redox processes. Interestingly, the incorporation of an adequate amount of cobalt into the nickel system has dramatically improved the charge storage ability as well as cycling stability owing to the synergistic effect between Ni and Co redox centers and the balanced charge storage phenomenon contributed by both the surface and intercalation redox processes. Especially, the material developed from $Ni_{60}Co_{40}$ 600 has exhibited a maximum specific capacitance of 566 F g^{-1} at 1 A g^{-1} current density and achieved an excellent capacitance retention of 84% (~99% coulombic efficiency) up to 10 000 cycles. Further, the corresponding hybrid device ($Ni_{60}Co_{40}$ 600//AC) has displayed an operational voltage window of 1.6 V and achieved a maximum energy density of 14.9 W h kg^{-1} at 794.5 W kg^{-1} power density and could retain ~86% of its initial capacity even after 25 000 cycles, thereby indicating the suitability of the electrode for practical applications.

Received 14th December 2023
Accepted 3rd January 2024

DOI: 10.1039/d3ta07761f

rsc.li/materials-a

Introduction

The modern world demands the inevitable use of energy storage systems (ESSs) in devices ranging from small electronic gadgets to heavy electric vehicles.[1–4] In this context, two potential candidates, *i.e.*, batteries and supercapacitors (SCs), are found to be promising owing to their high energy and power output, respectively.[5,6] Although SCs possess high power density, they still suffer from low specific energy compared to batteries.[7] To boost the energy density of SCs, the development of high specific capacity electrode materials and the construction of hybrid devices with a wide operational voltage window (V) is important.[8–10] In this context, battery-type electrodes are emerging as suitable alternatives due to their promising specific capacity compared to pseudo-capacitors and electrochemical double-layer capacitors (EDLCs).[11,12] These materials store charges through intercalation and surface redox processes.[13,14]

Recently, Ni-based materials have been vastly explored for SCs due to their relatively cheap, earth-abundant nature, and battery-like charge storage nature.[15] However, the poor cycling stability is a major bottleneck for Ni systems due to aggregation in longer cycles. Especially, nickel based sulfides (Ni_xS_y),[16,17] selenides (Ni_xSe_y),[18,19] phosphides (Ni_xP_y),[20,21] phosphates

[a]Department of Chemistry, Indian Institute of Science Education and Research (IISER), Mohanpur, Nadia, Kolkata, West Bengal, 741246, India. E-mail: mvenkataramanan@yahoo.com

[b]Department of Energy Science & Engineering, Daegu Gyeongbuk Institute of Science & Technology (DGIST), Daegu 42988, South Korea

† Electronic supplementary information (ESI) available. See DOI: https://doi.org/10.1039/d3ta07761f

$(Ni_x(PO_4)_y)$,[22] *etc.* delivered promising capacitance but suffer from poor cycling stability. There are a few reports that tried to enhance the cycling stability of the aforementioned materials. For instance, Nath *et al.* improved the cycling stability of nickel sulfide–nickel hydroxide structures by composite formation with thiophene and pyrrole-based copolymers.[23] The co-polymer improves the stability by limiting the aggregation of the active material. Further, the stability can be improved by tuning the morphology of Ni-based materials. Recently, Zhu and coworkers boosted up the cycling stability of flower-type $Ni(OH)_2$ particles through composite formation with ZnO flakes through electrodeposition.[24] In the composite structure, the individual ZnO and $Ni(OH)_2$ mutually prop each other, demonstrating excellent stability and morphology retention during a long run. In another report, Chen *et al.* demonstrated that cobalt incorporation in nickel selenide aids in the improvement of the cycling stability.[25] In this context, different Co based materials are found to be promising candidates for supercapacitors.[26,27] Especially, Co based LDHs[28,29] and oxyhydroxides[30] show excellent specific capacities and cycling stabilities.

Further, to improve charge storage, the development of highly porous electrodes with a larger number of metal centers is highly desired. In this context, electrochemical reconstruction of the precursor material is one of the ingenious strategies to enhance the electrochemical activity and stability. The reconstruction process is generally associated with the etching of functional moieties from the precursor materials during the electrochemical preconditioning process. The etching of the chemical groups (anionic and cationic) usually results in the exposure of more metal centers towards electrolytes and leads to facile transformation of metal precursors to their corresponding hydroxide/oxyhydroxide species. For instance, Liu *et al.* reported the transformation of trimetallic vanadium–cobalt–iron nitrides into their (oxy)hydroxide species by a surface reconstruction process *via* V etching.[31] Similarly, P etching assists in the conversion of a NiCoP pre-catalyst to Ni(Co)OOH active species by surface reconstruction during the water oxidation reaction.[32] In another report, Han *et al.* observed that cobalt iron phosphide displayed good electrochemical activity upon a bulk surface reconstruction process *via* etching of phosphorus.[33] Recently, our group has reported enhanced electrochemical activity due to porous hydroxide-(oxy)hydroxide formation by a structural reconstruction process *via* etching of phosphate and vanadate ions.[34,35] Yet, the etching-based reconstruction phenomenon is majorly limited for water oxidation catalysts and scarcely reported for supercapacitor applications. Our idea is to develop transition metal pyrophosphates and evaluate their potential for supercapacitor applications. Metal pyrophosphates ($M_xP_2O_7$) possess interesting structures and are evolving as promising candidates for SCs due to their cost effectiveness, wide operational voltage window, and high redox activity.[36] The presence of pyrophosphate units can make the materials more porous through the etching of anionic moieties during electrochemical cycling. Further, there are very few reports on pyrophosphate systems explored for energy storage applications. For instance, Senthilkumar *et al.* studied the aqueous hybrid device performance of $Ni_2P_2O_7$ and graphitic carbon, which displays a good operating voltage window of 1.6 V.[37] Similarly, Wang and co-workers developed a porous $Ni_2P_2O_7$ nanowire, which shows a good specific capacity of 772.5 F g^{-1}.[38] Despite achieving high specific capacities, the above systems lack in good cycling stability. Our idea is to introduce an appropriate amount of cobalt into nickel pyrophosphate to improve the capacity retention and stability. We presume that cobalt incorporation enhances the surface storage kinetics, thereby improving the cycling stability.

In this work, we have discussed the synthesis of amorphous nickel cobalt pyrophosphate ($P_2O_7^{4-}$) which upon electrochemical bulk structural reconstruction generates active nickel–cobalt hydroxide-(oxy)hydroxide *via* etching of pyrophosphate ions. A series of bimetallic pyrophosphates Ni_xCo_{100-x} 600 (x = 100, 90, 80, 70, 60, 50, 0) are prepared by the co-precipitation method using water and ethylene glycol as solvents followed by thermal annealing. Interestingly, the introduction of Co into the Ni system improved both the charge storage ability and retention rate by controlling both the intercalation and surface redox phenomena. Particularly, the material developed after the reconstruction of $Ni_{60}Co_{40}$ 600 manifests a maximum specific capacitance of 566 F g^{-1} at 1 A g^{-1} current density and a good capacitive retention of 84% up to 10 000 cycles. The transformation of $Ni_{60}Co_{40}$ 600 to Ni,Co(OOH) *via* phosphate etching and synergistic effects between Ni and Co centers was found to be the primary reason for the observed result. Further, a hybrid device was assembled using $Ni_{60}Co_{40}$ 600 and activated charcoal (AC). The hybrid device ($Ni_{60}C_{40}$ 600//AC) provides an operational voltage window of 1.6 V and delivers a maximum energy density of 14.9 W h kg^{-1} at 794.5 W kg^{-1} power density. Additionally, the $Ni_{60}C_{40}$ 600//AC device displayed excellent capacitive retention of 86% even after 25 000 cycles, indicating the potential of the developed material for practical applications.

Results and discussion

All the pyrophosphate materials were initially synthesized by a co-precipitation process using $Co(NO_3)_2 \cdot 6H_2O$, $NiCl_2 \cdot 6H_2O$, and $(NH_4)_2HPO_4$ as precursors. The above chemicals were dissolved in a water and ethylene glycol mixture and converted into ammonium metal hydrate. Subsequently, calcination at 600 °C results in desired pyrophosphate materials (see the details in the ESI†). For simplicity, the sample codes along with the Ni and Co ratio and the reaction temperature are summarized in Table 1.

Characterization

The phase information of the synthesized materials was identified by PXRD analysis. The diffraction patterns of as-prepared Co_{100} RT and Ni_{100} RT closely matched with the standard patterns of ammonium cobalt phosphate hydrate ($[NH_4]CoPO_4 \cdot H_2O$) (JCPDS No. # 01-089-6598) and ammonium nickel phosphate hydrate ($[NH_4]NiPO_4 \cdot 6H_2O$) (JCPDS No. # 00-021-0034), respectively (Fig. S1a†). Upon calcination, Co_{100} RT and Ni_{100} RT at 600 °C were converted into the corresponding pyrophosphate and denoted as Co_{100} 600 and Ni_{100} 600,

Table 1 Sample codes for the as-prepared pyrophosphate materials with different Ni/Co ratios and reaction conditions

Sample codes	Ni/Co	Reaction temperature
Co_{100} RT	0/100 (only Co)	Room temperature (RT)
Ni_{100} RT	100/0 (only Ni)	RT
$Ni_{60}Co_{40}$ RT	60/40	RT
Ni_{100} 600	100/0	600 °C
Co_{100} 600	0/100	600 °C
$Ni_{90}Co_{10}$ 600	90/10	600 °C
$Ni_{80}Co_{20}$ 600	80/20	600 °C
$Ni_{70}Co_{30}$ 600	70/30	600 °C
$Ni_{60}Co_{40}$ 600	60/40	600 °C
$Ni_{50}Co_{50}$ 600	50/50	600 °C

respectively. The PXRD pattern of Co_{100} 600 matched well with the monoclinic phase of $Co_2P_2O_7$ (JCPDS No. # 01-079-0825, $P2_1/c$ space group), whereas Ni_{100} 600 displayed amorphous nature (Fig. 1a). This observation has been reported previously.[37–40] Additionally, Ni_{100} RT was calcined at 800 °C, and the PXRD pattern of the resulting sample (Ni_{100} 800) matched with that of a pure phase of $Ni_2P_2O_7$ (JCPDS No. # 01-074-1604). The above results confirm that Ni_{100} 600 is very likely the amorphous phase of $Ni_2P_2O_7$. The amorphous nature of $Ni_{60}Co_{40}$ 600 might be caused by the presence of higher Ni content in the system. Similar diffraction patterns are observed for the samples prepared with varying Ni/Co ratios except for $Ni_{50}Co_{50}$ 600 which resembles the Co_{100} 600 pattern (Fig. S1b†). Further, thermogravimetric analysis (TGA) of Ni_{100} RT and $Ni_{60}Co_{40}$ RT gives information about calcination temperatures required for the pyrophosphate formation. The calculated mass loss up to 600 °C is around 26% and 26.54% for Ni_{100} RT and $Ni_{60}Co_{40}$ RT, respectively. This is maintained up to 800 °C in a static air atmosphere (Fig. S2†). The weight loss is associated with the elimination of ammonia and structural water molecules and results in the transformation of $[NH_4]NiPO_4 \cdot 6H_2O$ to $Ni_2P_2O_7$.[38,41,42] Furthermore, the PXRD pattern of the post TGA-analyzed Ni_{100} RT sample, denoted as Ni_{100} (post TGA), displays a small peak at ~29°, confirming the formation of $Ni_2P_2O_7$ (Fig. 1a). Subsequently, the chemical functional groups present in the materials were studied by Fourier-transformed infrared (FTIR) analysis. The FTIR spectra of Ni_{100} (post TGA) and all the annealed samples show two characteristic vibrational modes for PO_3 and P–O–P units (Fig. 1b and S3†). The band in the 1061–1084 cm^{-1} and 568–585 cm^{-1} regions can be attributed to PO_3 stretching and bending modes, respectively. In addition, a weak band noted in the 944–983 cm^{-1} region and a strong band appearing around the 737–752 cm^{-1} region are identified to be P–O–P bridge vibrations, confirming the presence of $P_2O_7^{4-}$.[43–46] To understand the porosity and surface area of the as-prepared materials, nitrogen adsorption desorption experiments were performed. Co_{100} 600, Ni_{100} 600, and $Ni_{60}Co_{40}$ 600 show a type-IV isotherm and H3 hysteresis loop, manifesting mesoporous nature and slit-like pore configuration in the materials (Fig. S4†).[47] The surface area values are found to be 32, 12, and 14 $m^2\ g^{-1}$ for Ni_{100} 600, Co_{100} 600, and $Ni_{60}Co_{40}$ 600, respectively. In addition, the pore size distribution (PSD) was analyzed from the BJH distribution (Fig. S5†). The measured pore diameters for Ni_{100} 600 and Co_{100} 600 are 7.6 nm and 2.1 nm, respectively. The above values further corroborate the feasibility of enhanced intercalation or diffusion of electrolyte ions in Ni_{100} 600 compared to Co_{100} 600. Notably, an adequate

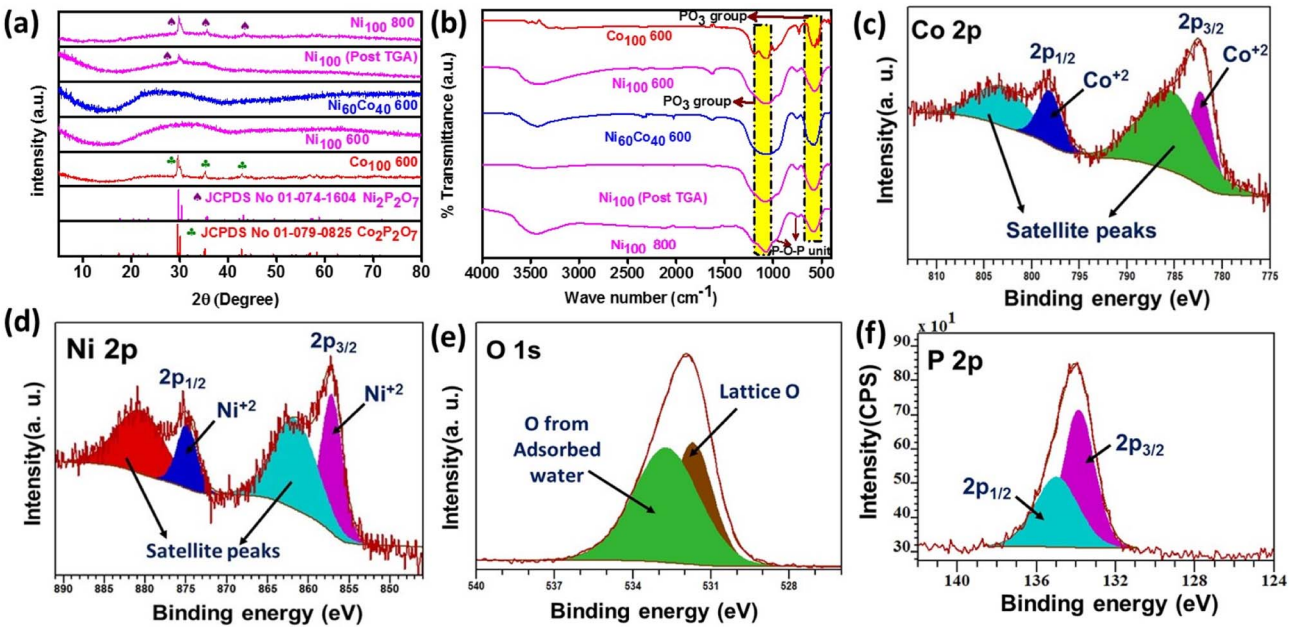

Fig. 1 (a) PXRD pattern and (b) FTIR spectra of Ni_{100} 600, Co_{100} 600, $Ni_{60}Co_{40}$ 600, Ni_{100} 800, and Ni_{100} (post TGA). The standard XRD patterns of $Ni_2P_2O_7$ (JCPDS No. # 01-074-1604) and $Co_2P_2O_7$ (JCPDS No. # 01-079-0825) are shown in (a). High-resolution XPS analysis of (c) Co 2p, (d) Ni 2p, (e) O 1s, and (f) P 2p for as-prepared $Ni_{60}Co_{40}$ 600.

quantity of Co introduction into the Ni system modulates the porosity in $Ni_{60}Co_{40}$ 600 (Table S1†). This helps regulate the charge storage mechanism by keeping the surface storage and intercalation phenomenon at an optimum level.

Chemical state analysis

The chemical state information of the elements present in $Ni_{60}Co_{40}$ 600 was obtained from X-ray photoelectron spectroscopic (XPS) analysis. The XPS survey scan of $Ni_{60}Co_{40}$ 600 confirms the presence of Ni, Co, O, and P elements in the material (Fig. S6†). Further, peak fitting of the Co 2p spectrum shows two main peaks positioned at 782.3 ($2p_{3/2}$) and 798.2 eV ($2p_{1/2}$). The binding energy (BE) difference of 15.9 eV between the peaks confirms the Co^{2+} state (Fig. 1c).[48,49] This is further supported by the characteristic satellite signals of Co^{2+} positioned at 785.6 and 803.4 eV. In the Ni 2p spectrum, the 857.2 and 874.9 eV peaks correspond to Ni $2p_{3/2}$ and $2p_{1/2}$, respectively. The noted peak separation of 17.7 eV suggests the presence of nickel in a +2 valence state (Fig. 1d).[50,51] Additionally, the characteristic satellite peaks for Ni 2p noted at 862 and 880.7 eV confirm that nickel is present as Ni^{2+}. The O 1s scan gives two peaks centered at 531.7 and 532.7 eV ascribed to lattice oxygen and adsorbed water molecules, respectively (Fig. 1e).[34] The peak fitted P 2p spectrum gives two peaks (due to spin–orbit splitting) at 134 and 134.9 eV for $2p_{3/2}$ and $2p_{1/2}$, respectively. The observed peak separation of about 0.9 eV indeed authenticates the presence of a pyrophosphate ligand in the precursor framework (Fig. 1f).[52] These aforementioned studies confirm the formation of bimetallic nickel cobalt pyrophosphate.

Morphological analyses

The morphology of the as-prepared materials was studied by field emission scanning electron microscopy (FESEM) and transmission electron microscopy (TEM). As shown in Fig. S7(a and b),† Co_{100} RT displays a hierarchical floret-like assembly, presumably formed through the self-assembly of micro-petals. Fig. S7(c and d)† display random floppy-kind architectures (size ~30–60 nm) for Ni_{100} RT. However, the observed morphology of $Ni_{60}Co_{40}$ RT is similar to that of Ni_{100} RT (Fig. S7(e and f)†). Further, the calcined samples show isotropic morphological conversion along with some cracks throughout the surface. These pores could be attributed to the elimination of structural water and ammonia molecules (supported by TGA analysis) (Fig. 2a and b). Further, the Ni-rich system retained its initial particle-like texture even after calcination at 600 °C (Fig. S8(a–d)†). Interestingly, upon calcination of $Ni_{60}Co_{40}$ RT, the initial particles are rearranged and transformed into interconnected network-like morphology with extended connectivity in $Ni_{60}Co_{40}$ 600 (Fig. 2c). Similar observation was made in the $Ni_{70}Co_{30}$ 600 material (Fig. S8(e and f)†). Meanwhile the $Ni_{50}Co_{50}$ 600 resembles Co_{100} 600 (Fig. S8(g and h)†). Further, the TEM analysis of $Ni_{60}Co_{40}$ 600 confirms the network-like morphology with long-range connectivity among the particles (Fig. 2(d–g)). EDS analysis corroborates the presence of Ni, Co, O, and P elements in $Ni_{60}Co_{40}$ 600 (Fig. 2h). In addition, the ICP-AES analysis shows that the Ni : Co ratio is 0.52 : 0.48 in the as-prepared $Ni_{60}Co_{40}$ 600 (Table S2†).

Electrochemical activation

The precursors were drop-cast on carbon paper and activated through electrochemical preconditioning using cyclic voltammetry (CV) at a 50 mV s^{-1} scan rate in the voltage window 0–0.65 V (*vs.* Ag/AgCl) in 1 M KOH (see the details in the ESI†). Interestingly, CV results show a continuous increase in the current density up to ~200 cycles for Ni_{100} 600, Co_{100} 600, and $Ni_{60}Co_{40}$ 600 (Fig. 3(a–c)). Especially an observable improvement in the current density is noticed in the 200th cycle compared to the 1st cycle (Fig. 3(d–f)). This can be attributed to the occurrence of major structural reconstruction during electrochemical preconditioning. For instance, Allam and coworkers have studied a bimetallic Ni–Co oxy phosphide

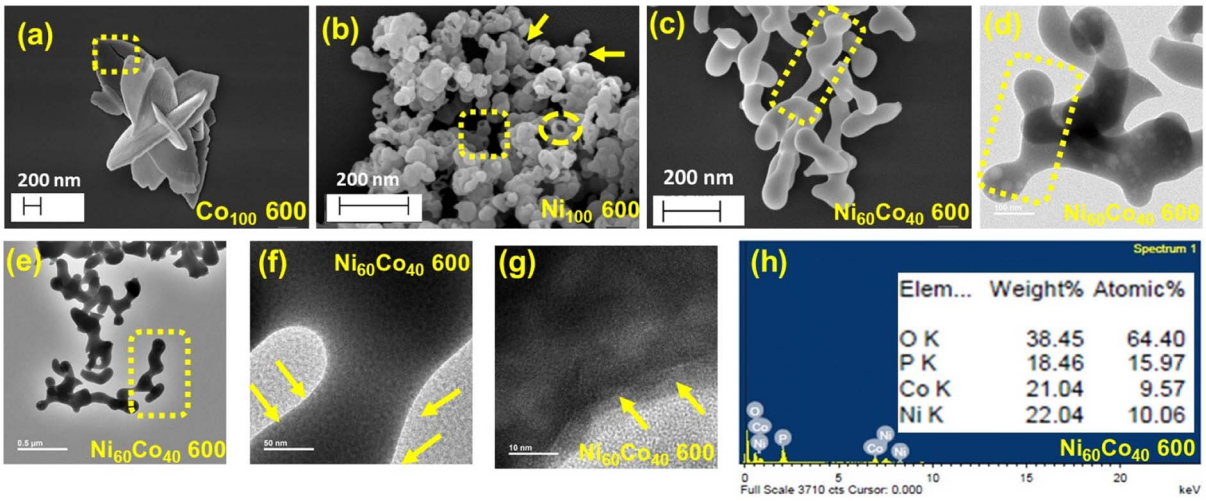

Fig. 2 FESEM images of as-prepared (a) Co_{100} 600, (b) Ni_{100} 600, and (c) $Ni_{60}Co_{40}$ 600, (d–g) TEM images and (h) EDS (Energy-dispersive X-ray spectroscopy) analysis for $Ni_{60}Co_{40}$ 600.

supercapacitor and emphasized the *in situ* generation of (oxy) hydroxide through structural reconstruction.[53] Further, during preconditioning, well-distinguished redox peaks characteristic of Co^{2+}/Co^{3+}, Co^{3+}/Co^{4+}, and Ni^{2+}/Ni^{3+} redox couples are observed with stepwise increment in the current density. The CV curves illustrate the faradaic nature of the charge storage and the exposure of more Ni and Co centers to the electrolyte during activation.[54,55] Similar results are observed for different compositions of Ni/Co optimized samples (Fig. S9†). The aforementioned results strongly suggest that metal pyrophosphates are likely converted into electrochemically active hydroxide-(oxy) hydroxide ($M(OH)_2$/MOOH) (M = Ni, Co) species mostly through surface reconstruction (*vide infra*). This phenomenon has been earlier reported during electrochemical processes in some electrocatalysts.[56] Among all the prepared materials, $Ni_{60}Co_{40}$ 600 manifests the maximum area under CV curves during electrochemical preconditioning. To optimize the electrolyte concentration, we have performed the CV and GCD tests of $Ni_{60}Co_{40}$ 600 in 0.5 M, 1 M and 2 M KOH electrolytes. We observed the highest redox current and maximum specific capacitance in 1 M KOH (Fig. S10†) and hence 1 M KOH was chosen for further electrochemical studies. To get more information, detailed structural analyses were performed on the electrochemically activated $Ni_{60}Co_{40}$ 600 sample.

Post preconditioning characterization

To examine the chemical state, morphology, and elemental content of $Ni_{60}Co_{40}$ 600 after preconditioning, *ex situ* studies like XPS, FESEM, HRTEM, and ICP-AES were performed. The XPS survey scan of the electrochemically activated $Ni_{60}Co_{40}$ 600 electrode material confirms the presence of Ni, Co, and O, and a trace amount of P after preconditioning (Fig. S11†). Further, the deconvoluted Co 2p spectrum shows peaks at 780.5 eV ($2p_{3/2}$) and 795.6 eV ($2p_{1/2}$). The noted BE difference of 15.1 eV between the two peaks corroborates Co^{3+} formation.[57] Additionally, the two peaks observed at 781.8 eV ($2p_{3/2}$) and 797.4 eV ($2p_{1/2}$) with a peak separation of ~16 eV suggest the presence of Co^{2+} (Fig. 4a).[47,58,59] Further, after activation, all Ni^{2+} centers transformed to Ni^{3+}, which was confirmed by the presence of characteristic Ni^{3+} peaks at 855.9 eV ($2p_{3/2}$) and 873.7 eV ($2p_{1/2}$) (Fig. 4b).[60] The peak fitted O 1s spectra display three peaks at 529.6, 531.3, and 532.6 eV, which are assigned to lattice oxygen, O from the hydroxyl group in an alkaline environment and adsorbed water molecules, respectively (Fig. 4c).[48,61] These observations further validate the formation of MOOH (M = Ni, Co) during the preconditioning process. Interestingly, the P 2p spectrum shows an observable decrease in phosphorus content compared to the as-prepared material (Fig. 4d). This implies the etching of P (likely as pyrophosphate) during preconditioning. Further ICP-AES analysis was performed with the electrolyte sequentially collected after 0, 25, 50, 100, 150, and 200 CV cycles of preconditioning for the $Ni_{60}Co_{40}$ 600 sample. Interestingly, the amount of P in the aliquots gradually increased from 0 to 150 cycles in the electrolyte. This observation confirms that P etches out likely as $P_2O_7^{4-}$ during the electrochemical preconditioning of the working electrode (Fig. S12 and Table S3†). Interestingly, electrochemical preconditioning results in a noticeable change in the morphology of the material. The FESEM study (on the carbon paper loaded material) on the electrochemically preconditioned $Ni_{60}Co_{40}$ 600 indicates that the initial network structure transformed into an agglomerated texture (Fig. S13†). Further, close inspection of TEM images revealed the formation of a porous flake-like morphology, which could be beneficial for better charge storage (Fig. 4e and f). The HRTEM image and its corresponding FFT pattern additionally

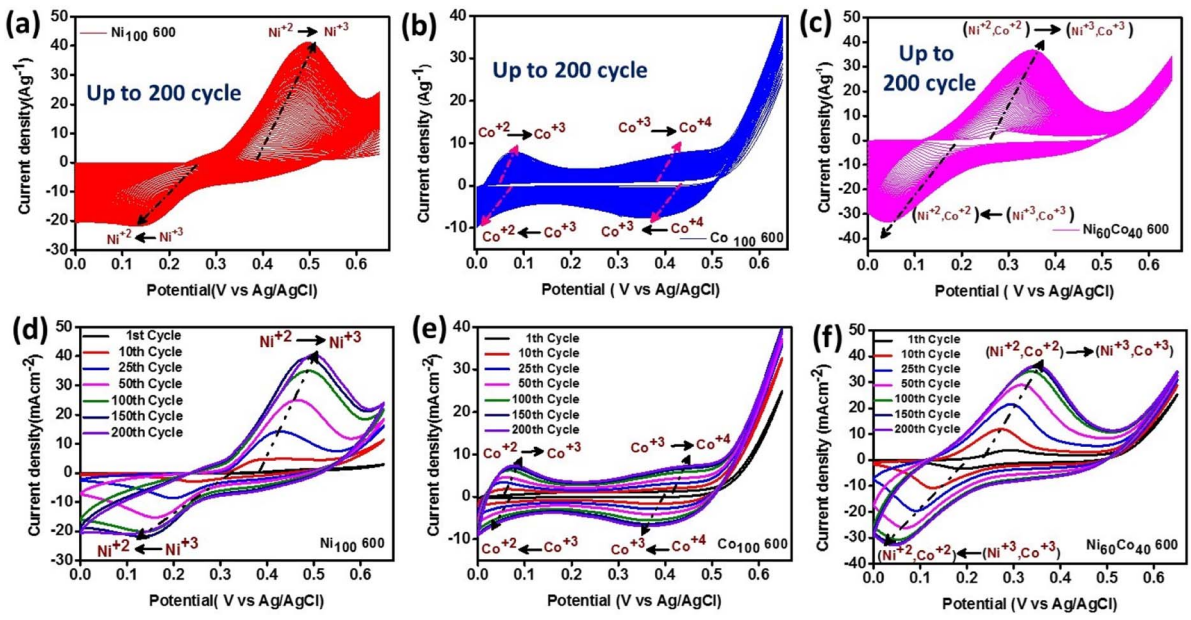

Fig. 3 CV curves indicate current density improvement during preconditioning (1 to 200 cycles) for (a and d) Ni_{100} 600, (b and e) Co_{100} 600 and (c and f) $Ni_{60}Co_{40}$ 600.

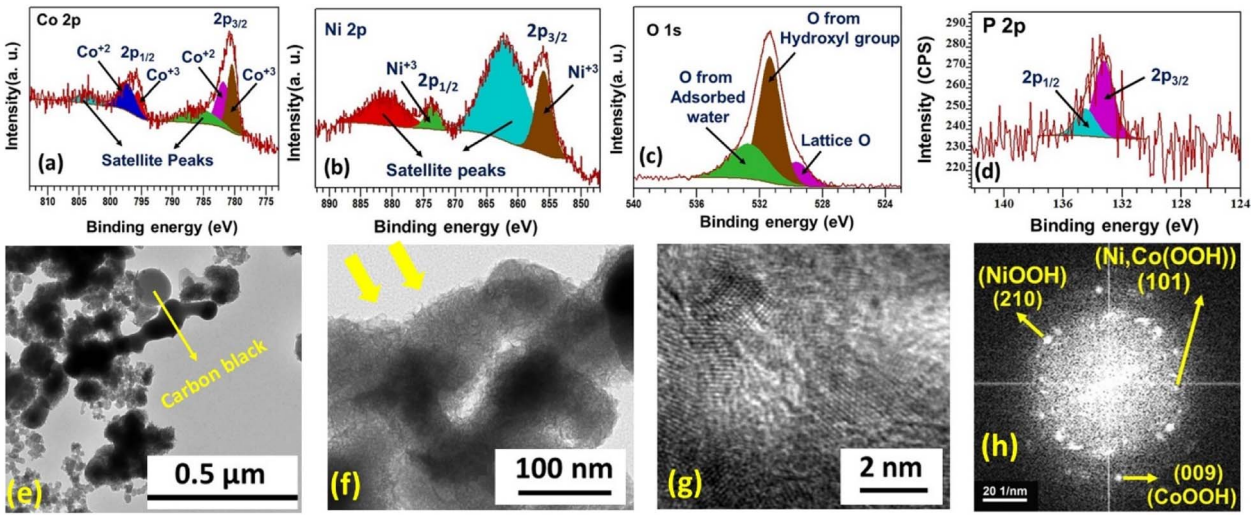

Fig. 4 XPS spectrum of (a) Co 2p, (b) Ni 2p, (c) O 1s, and (d) P 2p after preconditioning of $Ni_{60}Co_{40}$ 600, and (e and f) TEM images, (g) HRTEM image and (h) corresponding FFT pattern of $Ni_{60}Co_{40}$ 600 after electrochemical preconditioning. In the inset of figure (e), the sphere represents the carbon black used for the preparation of the working electrode.

support the existence of (210) and (009) planes characteristic of NiOOH (JCPDS No. # 00-027-0956) and CoOOH (JCPDS No. # 07-0169), respectively (Fig. 4g).[62,63] Moreover, the appearance of the (101) plane in the FFT pattern confirms the formation Ni,Co(OOH) in the activated material (Fig. 4h).[64,65] Based on our understanding and literature survey, we believe that the formation of Ni,Co hydroxide/(oxy)hydroxide from Ni,Co pyrophosphates is facilitated by the phosphate etching during the electrochemical process (detailed chemical mechanism is given in the ESI, page no. S24†).

Electrochemical performance of the activated material. The reconstructed materials (active materials) after electrochemical preconditioning were evaluated for supercapacitor performance. Initially, CV measurements of all the activated materials were recorded at a 5 mV s^{-1} scan rate (within 0–0.65 V *vs.* Ag/AgCl). The CV results reveal that the area under the CV curve for the sample Ni_{100} 600 is higher compared to the Co_{100} 600 sample demonstrating higher charge storage ability in the former (Fig. 5a). Upon Co incorporation the charge storage ability was altered. Especially, the material obtained after preconditioning of $Ni_{60}Co_{40}$ 600 displays maximum charge storage ability compared to Co_{100} 600, Ni_{100} 600, and all Ni/Co materials with different compositions (Fig. 5a and S14†). Further, the CVs of all activated materials were recorded at varying scan rates (5 to 50 mV s^{-1}). A significant increase in the redox current is noted for the activated $Ni_{60}Co_{40}$ 600 with increasing scan rate and the cathodic and anodic peaks shifted toward more negative and positive potential regions, respectively. The notable peak-to-peak gap at a high scan rate indicates that charge storage is principally diffusion-controlled (Fig. S15†). A similar behaviour was observed for all other materials with different Ni/Co compositions (Fig. S16†). Subsequently, the specific capacity (C_s) of all activated materials has been measured from their CV curves (see eqn (1) and (2), ESI†). Among all the materials, electrochemically activated $Ni_{60}Co_{40}$ 600 displays the highest C_s value. Further, with increasing scan rates, the C_s value decreases, which is attributed to insufficient time for the charge cumulation towards the electrode (Fig. 5b and S17†).[66] Meanwhile, the Co incorporation into the nickel system increased the capacitive retention rate. For example, the activated Co_{100} 600 and Ni_{100} 600 retained 72% and 44% of their initial specific capacity, respectively, at a 50 mV s^{-1} scan rate. Interestingly, after cobalt incorporation, the retention rate increased to 52% in $Ni_{60}Co_{40}$ 600 at the same scan rate (Fig. 5b).

Mechanism. Post Co incorporation into Ni systems, the observed increase in the area under the CV curve and redox current density is ascribed to the synergistic interaction of Ni and Co centers in the bimetallic system. This has enthused us to look into the mechanistic details of charge storage trajectory occurring in different electrochemically activated materials. This is done by calculating the *b* value, which is estimated from the slope of the log(peak current) *vs.* log (scan rate) plot using the power law (eqn (1) and (2)).[67]

$$i = av^b \quad (1)$$

$$\log(i) = \log(a) + b\log(v) \quad (2)$$

where v denotes the scan rate (mV s^{-1}), i is the cathodic (i_c) or anodic (i_a) peak current (mA), and a and b are variable parameters. The b value specifies the behaviour of charge storage. For example, when the b value is ~1, the $i(= i_c \text{ or } i_a)$ is linearly proportional to the scan rate ($i \propto v$), which signifies that the material stores the charge by a surface redox process (pseudo capacitor). Meanwhile, a b value of ~0.5 indicates intercalation redox or diffusion control behaviour (battery-type capacitor).[5] The estimated b values for Ni_{100} 600 and Co_{100} 600 are 0.5 and 0.98, indicating that charge storage mainly occurs through intercalation (battery-type) and surface redox (pseudocapacitive nature) processes, respectively. Interestingly, gradual incorporation of Co into the Ni system increases the b value successively

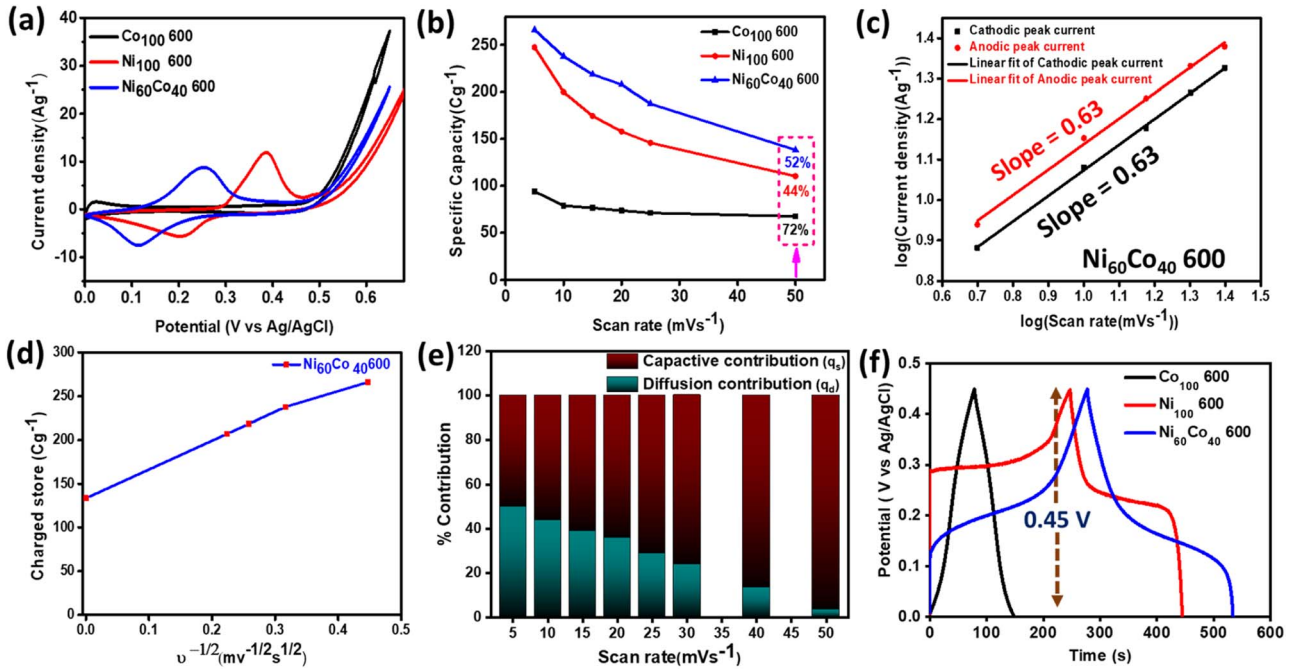

Fig. 5 (a) CV curves, (b) plot of C_s *vs.* scan rate for activated Ni_{100} 600, Co_{100} 600, and $Ni_{60}Co_{40}$ 600 samples, (c) *b* value estimation (within the 5 to 25 mV s^{-1} scan rate range), (d) C_s *vs.* $\nu^{-1/2}$ plot for activated $Ni_{60}Co_{40}$ 600, (e) the bar diagram showing % contribution from diffusion and capacitive processes at 5 to 50 mV s^{-1} scan rates and (f) GCD curves for Ni_{100} 600, Co_{100} 600, and $Ni_{60}Co_{40}$ 600 recorded at 1 A g^{-1}.

(Fig. S18).† This indicates that Co modulates the charge storage phenomenon by increasing the surface contribution to the Ni system.

Especially, the *b* value for the activated $Ni_{60}Co_{40}$ 600 is 0.63, suggesting that the material stores the charge through both intercalation and surface redox processes (Fig. 5c). Further, Trasatti's method was adopted to quantify both diffusion and capacitive contributions towards the charge storage of the materials. Generally, Trasatti's method correlates the diffusion (q_d) and surface (q_s) stored charges with varying scan rates. The total charge (q_t) accumulated under the CV curve is a combination of the capacitive component (q_s) and diffusive component (q_d) (eqn (3) and (4)).[68]

$$q_t = q_s + q_d \quad (3)$$

$$q_t = q_s + \text{const}\ \nu^{-1/2} \quad (4)$$

Normally, the q_s linearly varies with the scan rate (ν) due to quicker kinetics at the electrode surface compared to the bulk. On the other hand, the q_d component varies as the inverse square root of scan rate ($\nu^{-1/2}$). Generally, at a low scan rate due to sufficient time for diffusion, intercalation kinetics are dominant. Further, at a high scan rate ($\nu \rightarrow \infty$) the entire contribution predominately arises from the surface of the electrode (capacitive contribution).[69] Finally, the *y*-axis intercept from the q_t *vs.* $\nu^{-1/2}$ plot (at 5 to 20 mV s^{-1}) gives the information of q_s (Fig. 5d). Subsequently, the bulk contribution (q_d) is obtained by subtracting q_s from q_t. The contributions of q_s and q_d for Ni_{100} 600 and Co_{100} 600 are shown as a bar diagram in Fig. S19.† At a low scan rate (5 mV s^{-1}), Ni_{100} 600 and Co_{100} 600 show 79.4% and 42.6% diffusion contributions, respectively (Fig. S20†). These outcomes further support the inherent diffusion behaviour of the Ni system over the Co system and correlate with the estimated *b* value (*vide supra*). Interestingly, after the incorporation of an optimum quantity of Co into the Ni system, the activated $Ni_{60}Co_{40}$ 600 shows a 49.8% diffusion contribution (at a 5 mV s^{-1} scan rate). Further, at a high scan rates $Ni_{60}Co_{40}$ 600 displays 28.9% (25 mV s^{-1}) and only 3.5% (50 mV s^{-1}) diffusion contribution indicating predominant surface contribution towards the charge storage at a very high scan rate (Fig. 5e and S21).†

The galvanostatic charge–discharge (GCD) curves of all electrochemically activated materials were recorded at 1 A g^{-1} current density within the voltage window of 0–0.45 V. In the case of Ni_{100} 600, the GCD curve shows a long plateau, indicating battery-type charge storage or intercalation redox characteristics.[70] In contrast, Co_{100} 600 shows a quasi-triangular GCD profile suggesting surface redox or intrinsic pseudocapacitive behaviour. Interestingly, the GCD curve for $Ni_{60}Co_{40}$ 600 contains both a plateau and distorted quasi-triangular shape (Fig. 5f). Similar results are noticed for materials with different Ni/Co ratios (Fig. 6a). These results further support that Co incorporation into Ni systems results in both intercalation and surface contributions towards charge storage, *i.e.*, intercalation type pseudocapacitance (Fig. S22†).

Besides, the GCD profiles display a small *iR* drop associated with internal solution resistance and electrical contacts between the electrode and current outlets. Among the different activated materials, $Ni_{60}Co_{40}$ 600 delivered the maximum discharge time and highest specific capacitance (C_{sp}) value. The calculated C_{sp}

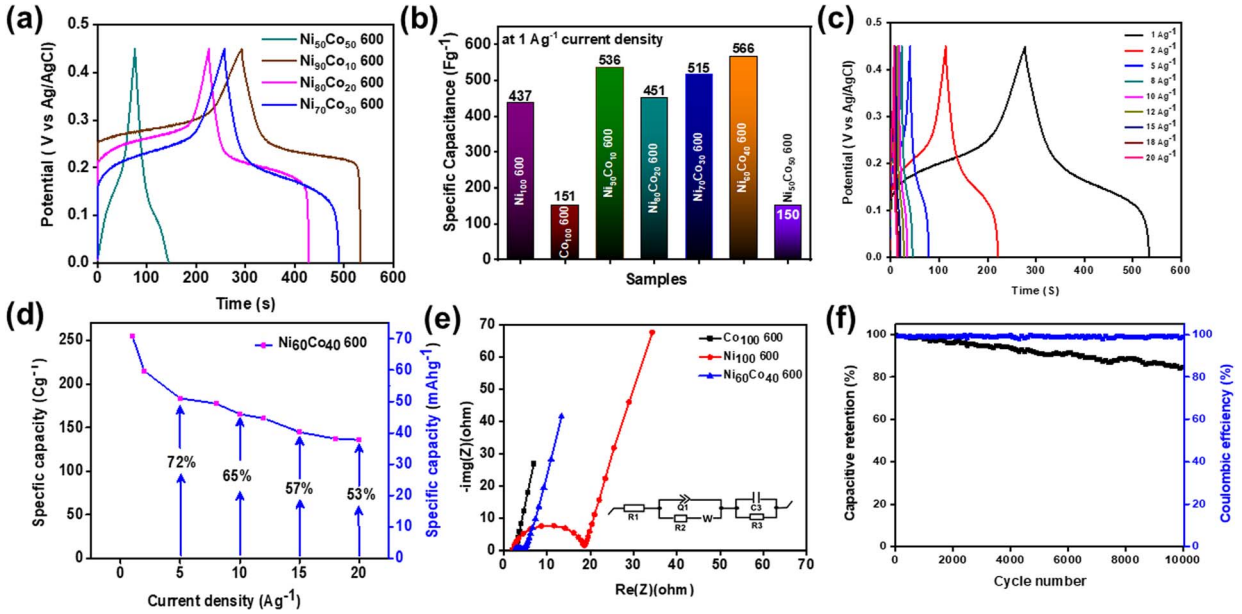

Fig. 6 (a) GCD curves (recorded within 0–0.45 V and 1 A g^{-1}), (b) bar diagram showing the C_{sp} for the as-prepared material with different Ni/Co ratios, (c) GCD curves of activated $Ni_{60}Co_{40}$ 600 at various current densities (1–20 A g^{-1}), (d) C_s *vs.* current density plot, (e) Nyquist plot for activated Ni_{100} 600, Co_{100} 600 and $Ni_{60}Co_{40}$ 600 (inset shows the Randles circuit for impedance data fitting, where *R*, *W*, *C*, and *Q* parameters are the resistor, Warburg impedance, capacitor, constant phase element, respectively), and (f) durability test of activated $Ni_{60}Co_{40}$ 600, performed at constant 10 A g^{-1} current density (up to 10 000 cycles).

values (recorded at 1 A g^{-1} current density) of the respective materials are shown as a bar diagram in Fig. 6b. Subsequently, the GCDs of all activated materials were measured at different current densities (1 to 20 A g^{-1}) (Fig. 6c and S23).† The calculated specific capacity (C_s) value of electrochemically activated $Ni_{60}Co_{40}$ 600 is 254.79 C g^{-1} (70.77 mA h g^{-1}) at 1 A g^{-1} current density. Further, with increasing current densities, the C_s values decreased (Fig. 6d and S24).† This is due to limiting diffusion time in a faster charge–discharge process.[71] On the other hand, the activated $Ni_{60}Co_{40}$ 600 could retain 72% of its initial capacity at 5 A g^{-1} current density and 53% at 20 A g^{-1} indicating the good rate capability of $Ni_{60}Co_{40}$ 600 (Fig. 6d). Further the diffusion and interfacial charge transfer resistance (R_{ct}) of the developed materials were monitored using electrochemical impedance spectroscopy (EIS) at the open circuit potential (OCP). The Nyquist plot of electrochemically activated Co_{100} 600, Ni_{100} 600, and $Ni_{60}Co_{40}$ 600 displays a semicircle and a vertical line in the high and low frequency zones, respectively (Fig. 6e). At high frequencies, the real axis intersection denotes equivalent series resistance (ESR) due to interfacial connections between the electrode material/current outlet and the inherent resistance of the electrolyte ions. At low frequency, the semicircle diameter and vertical line slope represent R_{ct} and Warburg impedance (Z_w) associated with diffusion kinetics, respectively.[68,72] Interestingly, after introduction of the requisite amount of Co, the semicircle diameter decreased in activated $Ni_{60}Co_{40}$ 600 compared to Ni_{100} 600. This observation indicates that cobalt incorporation into Ni systems helps in improving the charge transfer kinetics. Further, the observed ~70° slope of the vertical line for $Ni_{60}Co_{40}$ 600 manifests facile diffusion kinetics of electrolyte ions during charge storage.

Cycling stability is another important parameter to evaluate the suitability of the materials for supercapacitors. All the activated Ni/Co materials were subjected to continuous 5000 GCD cycles at 10 A g^{-1} current density. The activated Ni_{100} 600 shows only a 39% retention rate which suggests poor electrochemical robustness of the Ni system. Meanwhile Co_{100} 600 shows 96% capacitive retention indicating good stability (Fig. S25a†).

Interestingly, after gradual Co incorporation into the Ni system, cycling stability increases effectively. Especially, the activated $Ni_{60}Co_{40}$ 600 displays an excellent retention rate of 94% (up to 5000 cycles). The retention rate for other materials with different Ni/Co compositions is shown in Fig. S25b.† From the above results, a 3D scatter plot is drawn showing the *b* value (both cathodic and anodic) and % capacitive retention to understand the relationship between the charge storage procedure and stability (Fig. S26).†

The 3D plot further proves that gradual Co incorporation increases the *b* value and surface contribution to the overall charge storage process. In addition, the plot shows an increase in the stability of the Ni system with Co incorporation. Further, among all the activated materials, $Ni_{60}C_{40}$ 600 offers the best performance (Table S4).† This has encouraged us to extend the cycling stability test for longer cycles. The activated $Ni_{60}Co_{40}$ 600 shows a retention rate of 84% up to 10 000 cycles at 10 A g^{-1} current density and ~99% coulombic efficiency indicating excellent cycling stability and reversibility, respectively (Fig. 6f). The observed high stability value for $Ni_{60}Co_{40}$ 600 is found to be better compared to other reported pyrophosphate materials (see Table S7).† Further, the stability test indicates that the final

GCD curve shows only a little decrease in the plateau region as well as in the discharge time compared to the first cycle (Fig. S27 and S28).† This could be assigned to mild suppression of electrolyte migration channels present into the material during long GCD cycles.

Characterization after the electrochemical stability test

Meticulous physical characterization has been performed on the material after the stability studies. The XPS spectrum of the deconvoluted P 2p spectrum displays no characteristic signal indicating that the material's surface is devoid of any P (Fig. S29†). In addition, the P 2p XPS spectra of the as-prepared $Ni_{60}Co_{40}$ 600, after preconditioning treatment and post-stability measurement, are compared in Fig. 7a. The results clearly indicate the etching of P (likely as $P_2O_7^{4-}$) during preconditioning. In addition, the XPS study confirms the existence of Co^{2+} and Co^{3+} along with Ni^{3+} even after a long-term durability experiment (Fig. S30).†. The peak position values are shown in Table S5.† The post-stability Co, Ni 2p, and O 1s XPS spectra closely match the XPS results obtained after preconditioning, revealing the structural robustness of the activated material. The above results further indicate the possible formation of $M(OH)_2$/MOOH species (M = Ni, Co) in the post-stability material. Duan *et al.* demonstrated similar P etching through an electrochemical transformation from $FePO_4$ in a nickel rich system to NiFe-OOH.[73] Recently, Shreenivasa *et al.* noticed the absence of P in the post-XPS spectra owing to the surface reconstruction of $BiPO_4$ to Bi_2O_3.[74] Further, ICP-AES analysis of as-prepared $Ni_{60}Co_{40}$ 600, after preconditioning and post stability testing, further proves that the majority of P etching occurs from the as-prepared material during the preconditioning and hardly any change is noted after stability (Table S6).† The mechanism of the etching phenomenon is summarised and mentioned in

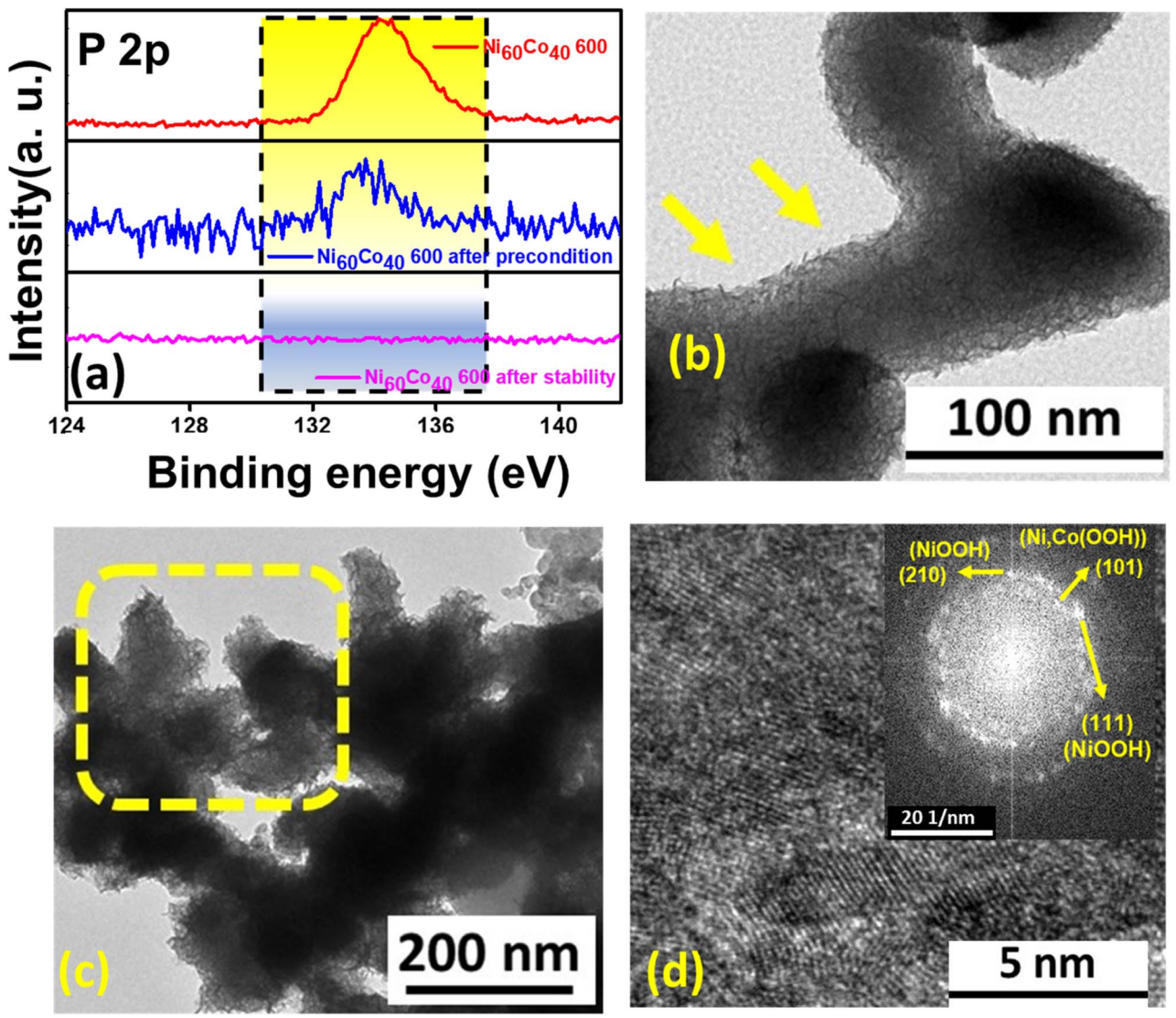

Fig. 7 (a) Comparison of total P intensity in the as-prepared material, after preconditioning and after stability testing, (b and c) TEM images, and (d) HRTEM image and corresponding FFT pattern (inset).

detail in the ESI.† The TEM images of the post stability $Ni_{60}Co_{40}$ 600 sample display retention of the porous flake-like morphology as acquired after preconditioning (Fig. 7(b and c)). Moreover, the HRTEM image and the corresponding FFT pattern show (210), (111), and (101) planes, which corroborates the formation of NiOOH and Ni,Co(OOH), respectively (Fig. 7d).[62,64,65,75] Further, the EDS study and elemental mapping analyses confirmed the presence of Co, Ni, O, and C (from the carbon paper substrate) and significant loss of P in the material after the extended durability test (Fig. S31).† The results above strongly support the formation of redox-active $M(OH)_2$/MOOH (M = Ni, Co) species through structural reconstruction of NiCo pyrophosphate.

Further, to understand the importance of Ni,Co hydroxides/oxyhydroxides derived through electrochemical reconstruction of the corresponding pyrophosphates, Ni,Co hydroxides were directly prepared (synthesis and characterisation are given in ESI page no. S22, Fig. S32 and S33†) and their activity was evaluated. The electrochemically activated $Ni_{60}Co_{40}$ 600 displays better reconstruction (Fig. S34(a–d))† and a higher area under the CV curve, compared to the as-synthesized hydroxides, manifesting better charge storage ability of the reconstructed material (Fig. S34e).† In addition, the GCD curves additionally support that activated $Ni_{60}Co_{40}$ 600 has a higher discharge time than the as-prepared Ni,Co hydroxide (Fig. S34f).† The calculated C_{sp} for Ni,Co hydroxide is 220 F g^{-1} (at 1 A g^{-1}), which is much lower than that of $Ni_{60}Co_{40}$ 600, indicating the suitability of pyrophosphate as an efficient precursor material for supercapacitor applications (Fig. S34g).†

Further, the PXRD analysis was performed on the carbon paper-supported material to unveil the phase formation at charged and discharged states. The broad diffraction peaks between ~36 and 39° and ~65 and 66.8° for the charged electrode indicate the formation of (Ni,Co(OOH)) (NiOOH JCPDS No. # 00-027-0956 and CoOOH JCPDS No. # 07-0169) (Fig. S35a).†.[76,77] In the case of the discharged electrode, the broad peaks observed between ~37 and 38.6° and ~61.4 and 63° suggest the formation of nickel cobalt hydroxide ($(Ni,Co(OH)_2)$) ($Ni(OH)_2$ JCPDS No. # 01-073-1520 and $Co(OH)_2$ JCPDS No. # 00-045-0031) (Fig. S35b).† Therefore, the proposed charged and discharged reaction could be attributed as follows (eqn (5) and (6)).

$$(Ni,Co(OH)_2) + OH^- \rightarrow (Ni,Co(OOH)) + H_2O + e^- \text{ (charging)} \quad (5)$$

$$(Ni,Co(OOH)) + H_2O + e^- \rightarrow (Ni,Co(OH)_2) + OH^- \text{ (discharging)} \quad (6)$$

Hybrid device performance

The noted high cycling stability and good charge storage capability of $Ni_{60}Co_{40}$ 600 motivated us to construct an asymmetric hybrid device. The hybrid device was fabricated in a two-electrode setup using $Ni_{60}Co_{40}$ 600 as the positive electrode and activated charcoal (AC) as the negative electrode (Fig. S36).† Initially, the CVs of positive and negative electrodes were separately recorded in a three-electrode setup. AC shows an EDLC nature, whereas activated $Ni_{60}Co_{40}$ 600 shows battery-type behaviour within their operational voltage window of −1 to 0 V and 0–0.6 V, respectively (Fig. 8a). Before constructing the device, the mass balance between positive and negative electrodes was maintained by the charge/mass balance equation (ESI†). Subsequently, a $Ni_{60}Co_{40}$ 600//AC hybrid device was

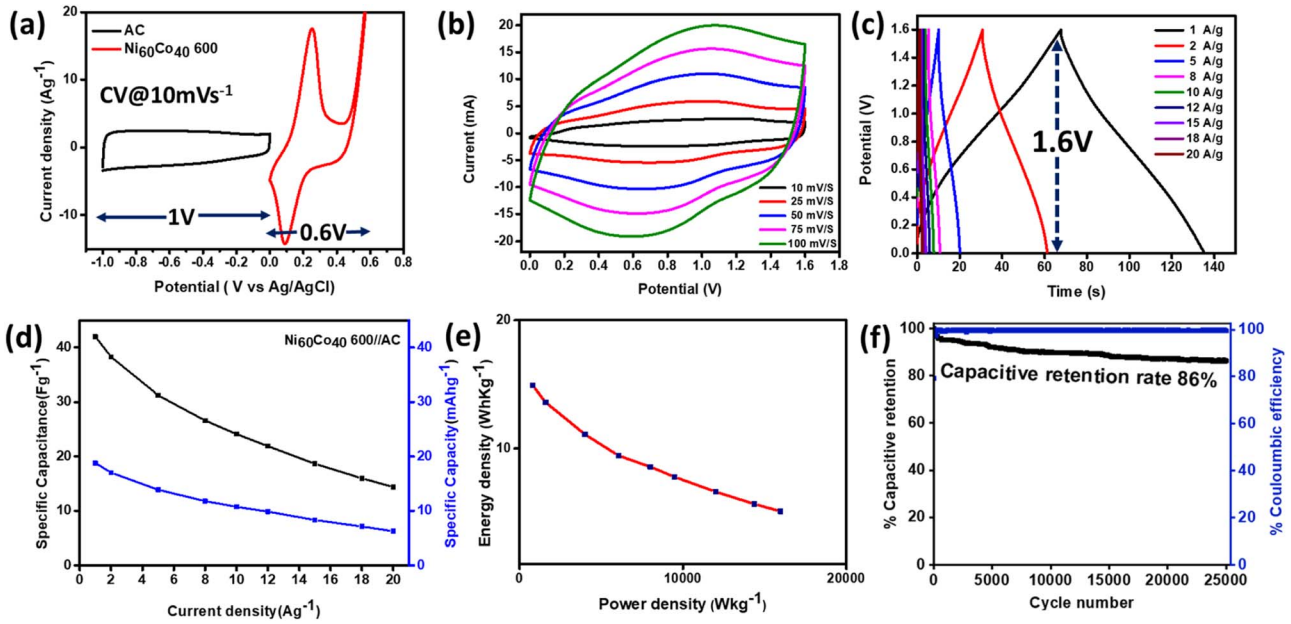

Fig. 8 CVs of AC and $Ni_{60}Co_{40}$ 600 measured in a 3-electrode setup, (b) CVs of the $Ni_{60}Co_{40}$ 600//AC hybrid device measured at varying scan rates, (c) GCD curves for $Ni_{60}Co_{40}$ 600//AC recorded at individual current density (within 0–1.6 V), (d) variation of C_{sp} and C_s *vs.* current density, (e) Ragone plot and (f) cycling stability test (at 10 A g^{-1} current density) of the hybrid device.

constructed with a series connection between $Ni_{60}Co_{40}$ 600 and AC. The voltage window of the hybrid device was determined by recording the CVs (5 mV s^{-1} scan rate) at 1.2 to 1.8 V. The CV result suggests that $Ni_{60}Co_{40}$ 600//AC has achieved a maximum operational voltage window of 1.6 V without any polarization (Fig. S37a).† The CVs of the hybrid device were recorded by varying the scan rates (10 to 100 mV s^{-1} within 0 to 1.6 V), which display both EDLC and redox behaviour (Fig. 8b).[78] The 1.6 V operational voltage window for the $Ni_{60}Co_{40}$ 600//AC hybrid device is further confirmed by recording the GCD in separate voltage windows (Fig. S37b).† Subsequently, the GCDs of the $Ni_{60}Co_{40}$ 600//AC hybrid device were collected at different current densities (1 to 20 A g^{-1}) at 1.6 V (Fig. 8c). The noted specific capacitance (specific capacity) value for the $Ni_{60}Co_{40}$ 600//AC device is 42 F g^{-1} (18.79 mA h g^{-1}) at 1 A g^{-1}, which could retain about 14.37 F g^{-1} (6.22 mA h g^{-1}) at 20 A g^{-1} current density, indicating a reasonable retention rate (Fig. 8d). The power and energy densities of the hybrid device were calculated from different GCD values (Fig. S38).† It is clear from the Ragone plot shown in Fig. 8e that the hybrid device displays a maximum of 14.9 W h kg^{-1} energy density at a power density of 794.5 W kg^{-1}. The value obtained for the carbon paper deposited substrate is quite comparable with values reported in the literature for other pyrophosphate-based materials (Table S8).† In addition, the hybrid device could retain 5.1 W h kg^{-1} energy density at a high-power density of 15 965.2 W kg^{-1}. Further, the hybrid device shows 86% capacitive retention and ~99% coulombic efficiency up to 25 000 GCD cycles, implying excellent cycling stability and good chemical reversibility (Fig. 8f). The comparison of the electrochemical activity, including long term stability performance of the developed $Ni_{60}Co_{40}$ 600//AC device with the reported pyrophosphate-based hybrid devices is illustrated in Table S8.† The data support the impressive cycling stability and capacitive retention of the $Ni_{60}Co_{40}$ 600//AC hybrid device compared to other systems, mainly using a cost-effective carbon substrate.

Conclusions

This work demonstrated an electrochemically induced surface reconstruction process for developing an efficient charge storage material. A simple co-precipitation process using different proportions of nickel and cobalt salts, followed by annealing, produced a series of amorphous bimetallic NiCo pyrophosphate precursors. Electrochemically induced reconstruction of the prepared bimetallic pyrophosphates resulted in the formation of highly porous Ni/Co hydroxide-(oxy)hydroxide species. Among the different pyrophosphate precursors, Ni-rich materials showed strong intercalation or battery-type charge storage behaviour and high specific capacitance compared to Co-rich systems. In contrast, the Co-rich system provides good cycling stability over the Ni system owing to predominant surface redox charge storage. Interestingly, introducing the requisite amount of Co into Ni systems improves the specific capacitance (due to the synergistic effect) and the cycling stability by modulating the intercalation and surface redox contribution towards the charge storage process. Particularly, the material obtained from the reconstruction of $Ni_{60}Co_{40}$ 600 showed a maximum specific capacitance of 566 F g^{-1} at 1 A g^{-1} current density through both intercalation and surface redox processes. Further, the material displayed 84% retention of its initial capacity after 10 000 cycles, suggesting good cycling stability. In addition, the $Ni_{60}C_{40}$ 600//AC hybrid device showed a maximum operational voltage window of 1.6 V with an energy density of 14.9 W h kg^{-1} at 794.5 W kg^{-1} power density. Further, the hybrid device retained 86% of its initial capacity after 25 000 cycles, suggesting excellent stability. These results indicate that the $Ni_{60}C_{40}$ 600//AC hybrid device is a potential candidate for practical applications. To our knowledge, this is the first detailed report on an electrochemically induced structurally reconstructed pyrophosphate material for supercapacitor applications. We strongly envision that the work unlocks the potential of the reconstruction strategy using transition metal pyrophosphates, which can be extended to other earth-abundant transitional metal-based pyrophosphate materials for energy storage applications.

Author contributions

A. R., H. R. Inta, and V. M. conceptualized the scheme of this work. A. R. carried out all the synthesis, total physical characterization, and entire electrochemical measurements. H. R. Inta, S. Ghosh, and V. M. constantly assisted A. R. during manuscript writing. A. M., H. V. S. R. M. Koppisetti, and B. R. Verma constantly aided A. R. in performing the HRTEM, FESEM, XPS, and ICP-AES studies. S. Bag, S. Ghosh, and A. R. performed the BET study. The whole work was supervised by V. M. together with valuable suggestions. Before submission, all authors have given assent to the final version of the manuscript.

Conflicts of interest

The authors reveal no conflict of interest.

Acknowledgements

A. R., Heramba V. S. R. M. Koppisetti, H. R. Inta, A. M., and B. R. Verma thank DST-inspire & CSIR, UGC, respectively, for their fellowship. S. Ghosh thanks SERB-N-PDF (PDF/2017/001728/ES). The author V. M. acknowledges DST, India (DST/TMD/MES/2K17/70) for the project funding. The authors thank IISER Kolkata for instrumental facilities, including HRTEM (DST-FIST facility). A. R. acknowledges SAIF, IIT Bombay for ICP-AES, and NIIST-Trivandrum for the XPS facility. A. R. also thanks Antarip Mitra, Viplove Mishra, Jaydeep Kumar, Khusboo S. Paliwal, Ashok Kumar Mahato, and Soumalya Debnath for their kind help and valuable suggestions.

Notes and references

1 M. S. Islam and C. A. J. Fisher, *Chem. Soc. Rev.*, 2014, **43**(1), 185–204.
2 E. Pomerantseva, F. Bonaccorso, X. Feng, Y. Cui and Y. Gogotsi, *Science*, 2019, **366**(6468), 969.

3 Z. S. Iro, C. Subramani and S. S. Dash, *Int. J. Electrochem. Sci.*, 2016, **11**, 10628–10643.
4 B. Y. Guan, L. Yu, X. Wang, S. Song and X. W. Lou, *Adv. Mater.*, 2017, **29**, 1605051.
5 D. P. Chatterjee and A. K. Nandi, *J. Mater. Chem. A*, 2021, **9**, 15880–15918.
6 V. Augustyn, P. Simon and B. Dunn, *Energy Environ. Sci.*, 2014, **7**(5), 1597–1614.
7 P. Simon, Y. Gogotsi and B. Dunn, *Science*, 2014, **343**, 1210–1211.
8 H. Khani and D. O. Wipf, *ACS Appl. Mater. Interfaces*, 2017, **9**, 6967–6978.
9 J.-C. Liu, Z.-H. Huang and T.-Y. Ma, *Small Struct.*, 2020, **1**, 2000020.
10 Y. Deng, Y. Ji, H. Wu and F. Chen, *Chem. Commun.*, 2019, **55**, 1486–1489.
11 B. Zhao, D. Chen, X. Xiong, B. Song, R. Hu, Q. Zhang, B. H. Rainwater, G. H. Waller, D. Zhen, Y. Ding, Y. Chen, C. Qu, D. Dang, C.-P. Wong and M. Liu, *Energy Storage Mater.*, 2017, **7**, 32–39.
12 J. Cherusseri, D. Pandey and J. Thomas, *Batter. Supercaps*, 2020, **3**, 860–875.
13 Y. Gogotsi and R. M. Penner, *ACS Nano*, 2018, **12**, 2081–2083.
14 J. S. Ko, C. H. Lai, J. W. Long, D. R. Rolison, B. Dunn and J. Nelson Weker, *ACS Appl. Mater. Interfaces*, 2020, **12**, 14071–14078.
15 W. Xu, X. Zhao, F. Zhan, Q. He, H. Wang, J. Chen, H. Wang, X. Ren and L. Chen, *Energy Storage Mater.*, 2022, **53**, 79–135.
16 Q. Xia, L. Si, K. Liu, A. Zhou, C. Su, N. M. Shinde, G. Fan and J. Dou, *Molecules*, 2023, **28**, 4307.
17 N. M. Santhosh, K. K. Upadhyay, P. Strazar, G. Filipic, J. Zavasnik, A. Mao de Ferro, R. P. Silva, E. Tatarova, M. F. Montemor and U. Cvelbar, *ACS Appl. Mater. Interfaces*, 2021, **13**, 20559–20572.
18 H. Reddy Inta, H. V. S. R. M. Koppisetti, S. Ghosh, A. Roy and V. Mahalingam, *ChemElectroChem*, 2023, **10**, 1–11.
19 S. Wu, Q. Hu, L. Wu, J. Li, H. Peng and Q. Yang, *J. Alloys Compd.*, 2019, **784**, 347–353.
20 D. Wang, L.-B. Kong, M.-C. Liu, W.-B. Zhang, Y.-C. Luo and L. Kang, *J. Power Sources*, 2015, **274**, 1107–1113.
21 Y. Jia, D. Hu, X. Wang, H. Zhang and P. Du, *J. Energy Storage*, 2022, **50**, 104713.
22 S. S. Patil, J. C. Shin and P. S. Patil, *Ceram. Int.*, 2022, **48**, 29484–29492.
23 A. R. Nath, B. Madhu, A. Mohan and N. Sandhyarani, *J. Energy Storage*, 2022, **46**, 103833.
24 M. Zhang, R. Zang, M. Zhang, R. Liu, X. Zhu, X. Li, H. Cui and H. Zhu, *J. Alloys Compd.*, 2022, **911**, 164865.
25 H. Chen, S. Chen, M. Fan, C. Li, D. Chen, G. Tian and K. Shu, *J. Mater. Chem. A*, 2015, **3**, 23653–23659.
26 X. Zhao, L. Mao, Q. Cheng, J. Li, F. Liao, G. Yang, L. Xie, C. Zhao and L. Chen, *Chem. Eng. J.*, 2020, **387**, 124081.
27 Y. Li, B. Huang, X. Zhao, Z. Luo, S. Liang, H. Qin and L. Chen, *J. Power Sources*, 2022, **527**, 231149.
28 B. Huang, W. Wang, T. Pu, J. Li, J. Zhu, C. Zhao, L. Xie and L. Chen, *J. Colloid Interface Sci.*, 2018, **532**, 630–640.
29 H. Wang, Q. He, F. Zhan and L. Chen, *J. Colloid Interface Sci.*, 2023, **630**, 286–296.
30 H. Wang, X. Ren, J. Chen, W. Xu, Q. He, H. Wang, F. Zhan and L. Chen, *J. Power Sources*, 2023, **554**, 232309.
31 D. Liu, H. Ai, J. Li, M. Fang, M. Chen, D. Liu, X. Du, P. Zhou, F. Li, K. H. Lo, Y. Tang, S. Chen, L. Wang, G. Xing and H. Pan, *Adv. Energy Mater.*, 2020, **10**(45), 1–9.
32 W. Zou, C. Sun, K. Zhao, J. Li, X. Pan, D. Ye, Y. Xie, W. Xu, H. Zhao, L. Zhang and J. Zhang, *Electrochim. Acta*, 2020, **345**, 136114.
33 X. Han, C. Yu, Y. Niu, Z. Wang, Y. Kang, Y. Ren, H. Wang, H. S. Park and J. Qiu, *Small Methods*, 2020, **4**, 1–10.
34 R. Kumar, H. R. Inta, H. V. S. R. M. Koppisetti, S. Ganguli, S. Ghosh and V. Mahalingam, *ACS Appl. Energy Mater.*, 2020, **3**, 12088–12098.
35 A. Mondal, S. Ganguli, H. R. Inta and V. Mahalingam, *ACS Appl. Energy Mater.*, 2021, **4**, 5381–5387.
36 S. S. Patil and P. S. Patil, *Chem. Eng. J.*, 2023, **455**, 140639.
37 B. Senthilkumar, Z. Khan, S. Park, K. Kim, H. Ko and Y. Kim, *J. Mater. Chem. A*, 2015, **3**, 21553–21561.
38 Y. Zhou, C. Liu, X. Li, L. Sun, D. Wu, J. Li, P. Huo and H. Wang, *J. Alloys Compd.*, 2019, **790**, 36–41.
39 P. Suganya, A. Venkadesh, J. Mathiyarasu and S. Radhakrishnan, *J. Solid State Electrochem.*, 2019, **23**, 3429–3435.
40 A. G. Meguerdichian, T. Jafari, M. R. Shakil, R. Miao, L. A. Achola, J. Macharia, A. Shirazi-Amin and S. L. Suib, *Inorg. Chem.*, 2018, **57**, 1815–1823.
41 H. Pang, Y.-Z. Zhang, Z. Run, W.-Y. Lai and W. Huang, *Nano Energy*, 2015, **17**, 339–347.
42 C. Wei, C. Cheng, S. Wang, Y. Xu, J. Wang and H. Pang, *Chem.–Asian J.*, 2015, **10**, 1731–1737.
43 N. Zhang, C. Chen, Y. Chen, G. Chen, C. Liao, B. Liang, J. Zhang, A. Li, B. Yang, Z. Zheng, X. Liu, A. Pan, S. Liang and R. Ma, *ACS Appl. Energy Mater.*, 2018, **1**(5), 2016–2023.
44 B. Boonchom and N. Vittayakorn, *Mater. Lett.*, 2010, **64**, 275–277.
45 V. Ramakrishnan, S. N. Kalkura and P. Rajagopal, *Pramana*, 1990, **34**, 555–560.
46 A. Ait Salah, F. Gendron, K. Zaghib, M. M. K. Benkhaouja and C. M. Julien, *J. Electrochem. Soc. Proc.*, 2008, **14**, 165–172.
47 S. Ghosh, A. Mondal, G. Tudu, S. Ghosh, H. V. S. R. M. Koppisetti, H. R. Inta, D. Saha and V. Mahalingam, *ACS Sustain. Chem. Eng.*, 2022, **10**(22), 7265–7276.
48 S. Ghosh, R. Jana, S. Ganguli, H. R. Inta, G. Tudu, H. Koppisetti, A. Datta and V. Mahalingam, *Nanoscale Adv.*, 2021, **3**, 3770–3779.
49 M. Mgolombane, O. M. Bankole, E. E. Ferg and A. S. Ogunlaja, *Mater. Chem. Phys.*, 2021, **268**, 124733.
50 S. Ghosh, H. R. Inta, M. Chakraborty, G. Tudu, H. V. S. R. M. Koppisetti, K. S. Paliwal, D. Saha and V. Mahalingam, *ACS Appl. Nano Mater.*, 2022, **5**, 7246–7258.
51 H. Li, Y. Yu, M. B. Starr, Z. Li and X. Wang, *J. Phys. Chem. Lett.*, 2015, **6**, 3410–3416.
52 R. Mahajan, R. Prakash, R. J. Choudhary and D. M. Phase, *Phys. Scr.*, 2021, **96**(7), 075808.

53 A. A. Saleh, D. M. Sayed, L. A. V. Nagle-Cocco, G. Divitini, L. G. Ghanem, C. Ducati and N. K. Allam, *ACS Appl. Energy Mater.*, 2022, **5**(6), 7661–7673.
54 Y.-T. Lu, Y.-J. Chien, C.-F. Liu, T.-H. You and C.-C. Hu, *J. Mater. Chem. A*, 2017, **5**(39), 21016–21026.
55 B. Lu, D. Cao, P. Wang, G. Wang and Y. Gao, *Int. J. Hydrogen Energy*, 2011, **36**(1), 72–78.
56 A. Sivanantham, P. Ganesan, A. Vinu and S. Shanmugam, *ACS Catal.*, 2020, **10**(1), 463–493.
57 C. Yuan, H. G. Wang, J. Liu, Q. Wu, Q. Duan and Y. Li, *J. Colloid Interface Sci.*, 2017, **494**, 274–281.
58 A. Mondal, H. R. Inta, A. Roy, A. Kumar Mahato and V. Mahalingam, *ACS Appl. Nano Mater.*, 2023, **6**, 12040–12049.
59 C. Alex, S. C. Sarma, S. C. Peter and N. S. John, *ACS Appl. Energy Mater.*, 2020, **3**(6), 5439–5447.
60 H. R. Inta, S. Ghosh, A. Mondal, G. Tudu, H. V. S. R. M. Koppisetti and V. Mahalingam, *ACS Appl. Energy Mater.*, 2021, **4**(3), 2828–2837.
61 H. V. S. R. M. Koppisetti, S. Ganguli, S. Ghosh, H. R. Inta, G. Tudu and V. Mahalingam, *ACS Appl. Energy Mater.*, 2022, **5**(2), 1681–1689.
62 Q. Zhang, C. Zhang, J. Liang, P. Yin and Y. Tian, *ACS Sustain. Chem. Eng.*, 2017, **5**(5), 3808–3818.
63 Q. Song, J. Wang, Q. Sun, X. Wang, Z. Zhu, C. Pei, H. Li, Z. Luo, X. Huang and W. Huang, *Chem. Commun.*, 2020, **56**(71), 10285–10288.
64 Z. Y. Wang, L. Wang, S. Liu, G. R. Li and X. P. Gao, *Adv. Funct. Mater.*, 2019, **29**, 1901051.
65 X. Liu, K. Ni, B. Wen, R. Guo, C. Niu, J. Meng, Q. Li, P. Wu, Y. Zhu, X. Wu and L. Mai, *ACS Energy Lett.*, 2019, **4**, 2585–2592.
66 S. J. Marje, P. R. Deshmukh, J. L. Gunjakar, C. D. Lokhande and U. M. Patil, *Energy Fuels*, 2021, **35**(17), 14110–14121.
67 K. Wang, S. Wang, J. Liu, Y. Guo, F. Mao, H. Wu and Q. Zhang, *ACS Appl. Mater. Interfaces*, 2021, **13**, 15315–15323.
68 T. S. Mathis, N. Kurra, X. Wang, D. Pinto, P. Simon and Y. Gogotsi, *Adv. Energy Mater.*, 2019, **9**, 1–13.
69 S. Kaipannan, K. Govindarajan, S. Sundaramoorthy and S. Marappan, *ACS Omega*, 2019, **4**, 15798–15805.
70 K. V. Sankar, Y. Seo, S. C. Lee and S. Chan Jun, *ACS Appl. Mater. Interfaces*, 2018, **10**, 8045–8056.
71 G. Nagaraju, G. S. Raju, Y. H. Ko and J. S. Yu, *Nanoscale*, 2016, **8**, 812–825.
72 S. S. Rabbani, H. Mustafa, A. Zafar, S. Javaid, M. A. Bakar, A. Nisar, Y. Liu, S. Karim, H. Sun, S. Hussain, Z. Zafar, Y. Faiz, F. Faiz, Y. Yu and M. Ahmad, *Electrochim. Acta*, 2023, **446**, 142098.
73 R. Duan, Y. Li, S. Wang, J. Gong, Y. Tong and W. Qi, *J. Phys. Chem. Lett.*, 2022, **13**, 1446–1452.
74 L. Shreenivasa, A. Siddaramanna, Y. Kalegowda, A. Syed, N. Marraiki and P. S. Adarakatti, *Solid State Sci.*, 2022, **124**, 106803.
75 J. Liu, W. Qiao, Z. Zhu, J. Hu and X. Xu, *Small*, 2022, **18**, 2202434.
76 M. Gao, Y. Li, J. Yang, Y. Liu, Y. Liu, X. Zhang, S. Wu and K. Cai, *Chem. Eng. J.*, 2022, **429**, 132423.
77 S. Ganguli, S. Ghosh, G. Tudu, H. Koppisetti and V. Mahalingam, *Inorg. Chem.*, 2021, **60**, 9542–9551.
78 C. Lu, Y. Yan, T. Zhai, Y. Fan and W. Zhou, *Batter. Supercaps*, 2020, **3**, 534–540.